nature portfolio

https://doi.org/10.1038/s41563-021-01183-0

Supplementary information

Tandem catalysis with double-shelled hollow spheres

In the format provided by the authors and unedited

Supplementary Information for

Tandem Catalysis with Double-Shelled Hollow Spheres

Jiadong Xiao,[1,4,8] Kang Cheng,[2,8] Xiaobin Xie,[3,5] Mengheng Wang,[2] Shiyou Xing,[1] Yuanshuai Liu,[1,6] Thomas Hartman,[1] Donglong Fu,[1,7] Koen Bossers,[1] Marijn A. van Huis,[3] Alfons van Blaaderen,[3] Ye Wang[2,*] and Bert M. Weckhuysen[1,*]

[1] Inorganic Chemistry and Catalysis, Debye Institute for Nanomaterials Science, Utrecht University, Universiteitsweg 99, 3584 CG Utrecht, the Netherlands

[2] State Key Laboratory of Physical Chemistry of Solid Surfaces, College of Chemistry and Chemical Engineering, Xiamen University, Xiamen, China

[3] Soft Condensed Matter, Debye Institute for Nanomaterials Science, Utrecht University, Princetonplein 5, 3584 CC Utrecht, the Netherlands

[4] Present address: Research Initiative for Supra-Materials, Interdisciplinary Cluster for Cutting Edge Research, Shinshu University, 4-17-1 Wakasato, Nagano-shi, Nagano 380-8553, Japan

[5] Present address: Electron Microscopy for Materials Science (EMAT), University of Antwerp, Groenenborgerlaan 171, B-2020 Antwerp, Belgium

[6] Present address: Qingdao Institute of Bioenergy and Bioprocess Technology, Chinese Academy of Sciences, Qingdao 266101, China

[7] Present address: Chemistry and Chemical Engineering, California Institute of Technology, Pasadena, California 91125, United States of America

[8] These authors contributed equally to this work

*Email: B.M.Weckhuysen@uu.nl (B.M.W.)

wangye@xmu.edu.cn (Y.W.)

Table of contents

Supplementary Table 1. Zeta-potentials of materials in aqueous solutions.

Material	ζ-Potential/mV
CSs[a]	−18.9 ± 0.3
Fe^{3+}-CSs[a]	−13.5 ± 1.1
S-1 nanocrystal[b]	−14.4 ± 1.1

[a] 1 g L^{-1} in distilled water; [b] 1 wt% of sample was dispersed in distilled water.

Note: Although the Fe^{3+} doping treatment of CSs (ζ-potential = −18.9 mV) neutralized to some degree the negative surface charge of CSs, the resultant Fe^{3+}-CSs (ζ-potential = −13.5 mV) still exhibited negatively charged surfaces. The change in surface charge was minor, possibly because CSs adsorbed also a similar number of nitrate anions, as we also detected N species within Fe^{3+}-CSs by the STEM-EDS analysis (Supplementary Fig. 1). Negatively charged CSs with abundant −OH and −C=O groups on surface (Supplementary Fig. 10) tend to adsorb oxygen-containing anions (e.g., NO_3^-) because of the similar elemental composition[1], which promotes further the adsorption of Fe^{3+} cations through electrostatic attractions.

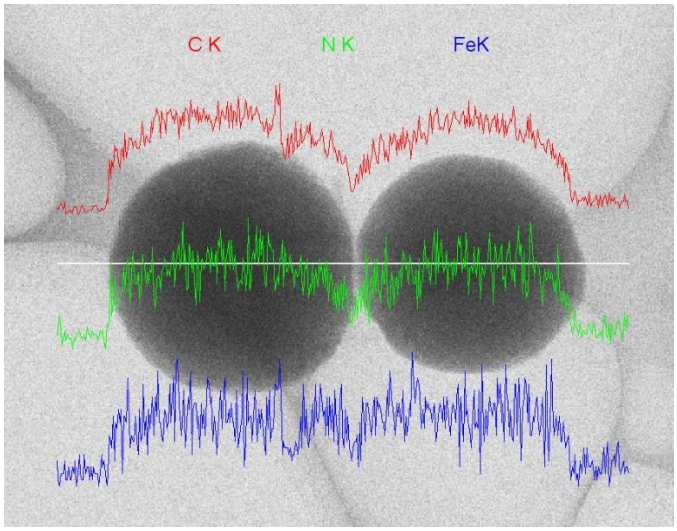

Supplementary Fig. 1: EDS line scan of C, N and Fe elements in Fe^{3+}-CSs.

Note: Owing to the electrostatic attraction between the positively charged Fe^{3+} cations and negatively charged CSs (ζ-potential = −18.9 mV, Supplementary Table 1) and the existing nanopores of CSs,[2] Fe^{3+} cations traveled into and resided throughout the CSs interior. The EDS curves of N and Fe elements exhibited the same spherical shape as that of C element, indicating that the adsorbed nitrates and Fe^{3+} species inside Fe^{3+}-CSs are almost evenly distributed. Note that this EDS measurement was specially performed on a Hitachi HD-2300A STEM.

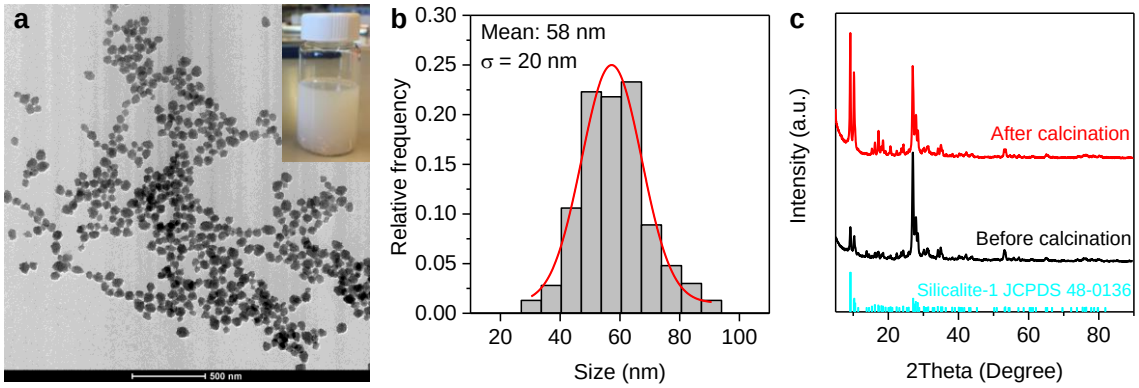

Supplementary Fig. 2: Characterization of the prepared S-1 nanocrystals. (a) TEM image, (b) size distribution with the estimated mean size, and (c) XRD patterns of S-1 nanocrystals before and after calcination in air. The inlet in panel **a** shows the photograph of 1 wt% S-1 nanocrystal suspension in distilled water.

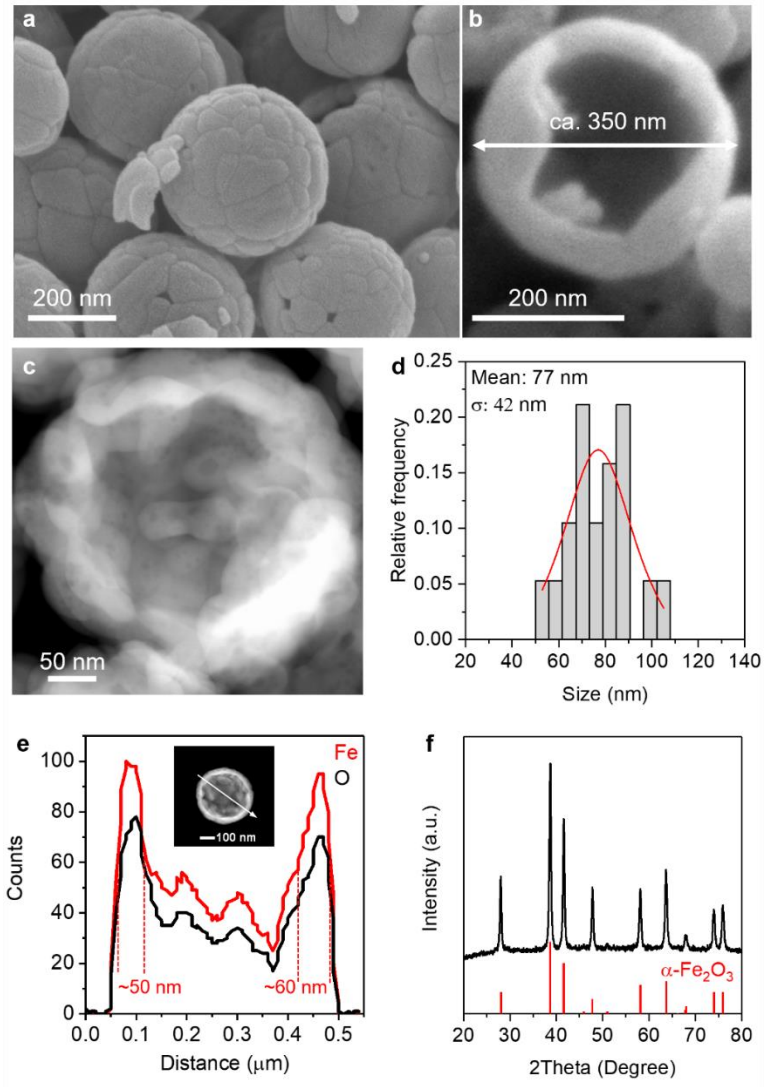

Supplementary Fig. 3: Characterization of single-shelled hollow Fe_2O_3 spheres (hs-Fe_2O_3) prepared by direction calcination of Fe^{3+}-CSs in air. (a and b) SEM and (c) STEM-HAADF images of hs-Fe_2O_3. (d) estimation of the average Fe_2O_3 crystal size of the longest dimension in hs-Fe_2O_3. (e) Fe and O EDS line-scan spectra, and (f) XRD patterns of hs-Fe_2O_3.

Note: Calcining Fe^{3+}-CSs in air directly generated single-shelled hollow α-Fe_2O_3 spheres with diameters of ca. 350 nm and thicknesses of 50−60 nm. Although the average α-Fe_2O_3 crystal size of the longest dimension was 77 nm, the S_{BET} of hs-Fe_2O_3 reached as high as 61.2 m^2/g (Supplementary Table 3) due to the unique hollow-sphere structure composed of cambered-tile-like α-Fe_2O_3 crystals. Note that the Fe_2O_3 component in the hollow Fe_2O_3 sphere@S-1 colloidal particles and Fe_2O_3@S-1(ZSM-5) DSHSs was the same as the hs-Fe_2O_3 here.

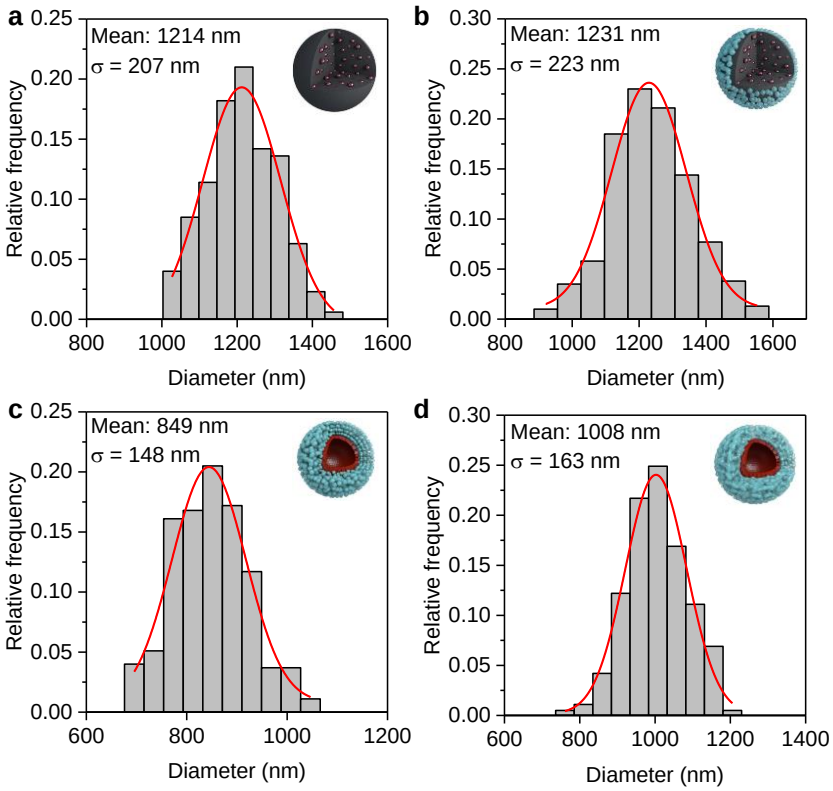

Supplementary Fig. 4: Size distribution and the estimated mean diameters of different materials based on their SEM images. (a) Fe^{3+}-CSs, (b) Fe^{3+}-CS@S-1 colloids, (c) hollow Fe_2O_3 sphere@S-1 colloids, and (d) Fe_2O_3@S-1 DSHSs. Gaussian distribution was used for the estimation of the mean size.

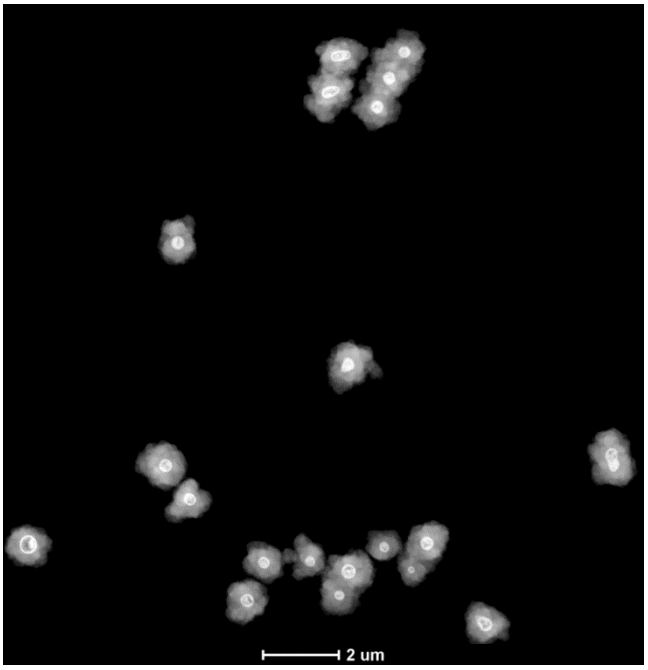

Supplementary Fig. 5: STEM-HAADF image of Fe_2O_3@S-1 DSHSs.

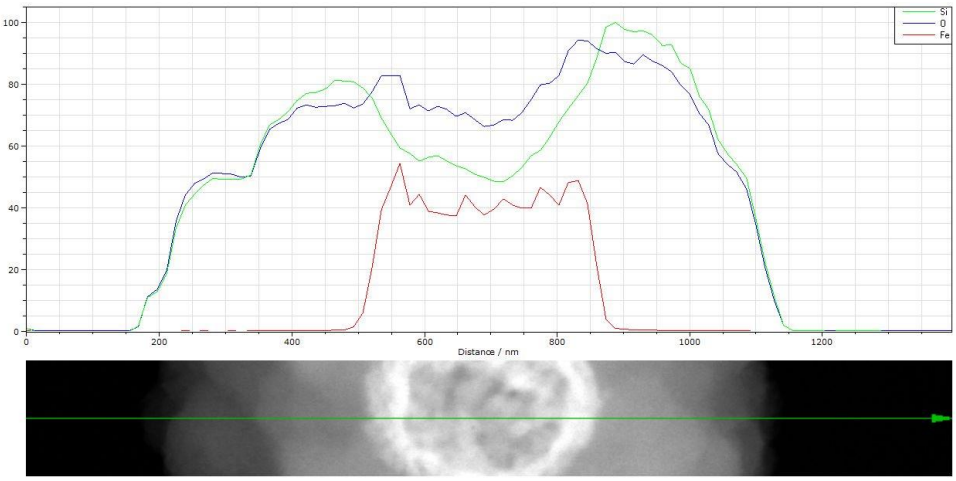

Supplementary Fig. 6: STEM-EDS line-scan spectra of Si, O, and Fe elements in Fe_2O_3@S-1 DSHSs. This clearly indicates that the a Fe_2O_3@S-1 DSHS particle comprises a hollow Fe_2O_3 sphere as the inner shell and a hollow S-1 sphere as the outer shell.

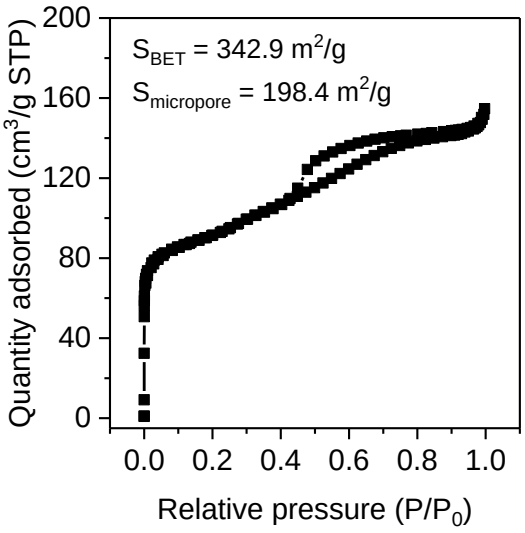

Supplementary Fig. 7: Nitrogen adsorption-desorption isotherm of Fe_2O_3@S-1 DSHSs. The micropore area was determined by the t-plot method.

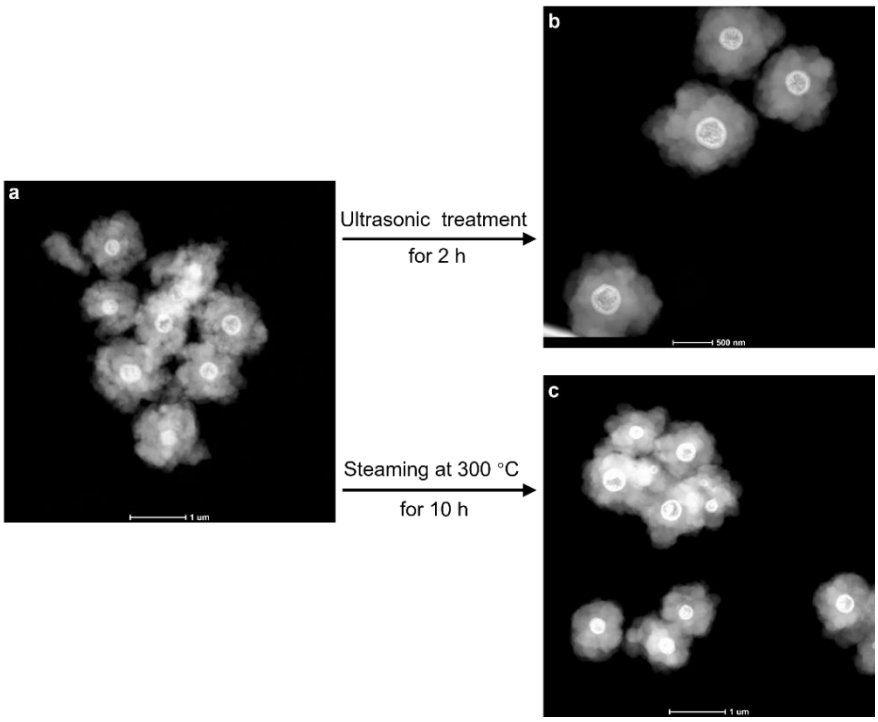

Supplementary Fig. 8. Effect of ultrasonic and steaming treatment on the structural stability of Fe_2O_3@S-1 DSHSs. STEM-HAADF images of Fe_2O_3@S-1 DSHSs (the material in Supplementary Fig. 12c) (a) without any treatment, and with (b) ultrasonic treatment (300 W, 28 kHz) for 2 h or (c) steaming treatment (H_2O-containing N_2 flow: 40 mL min^{-1}) at 300 °C for 10 h.

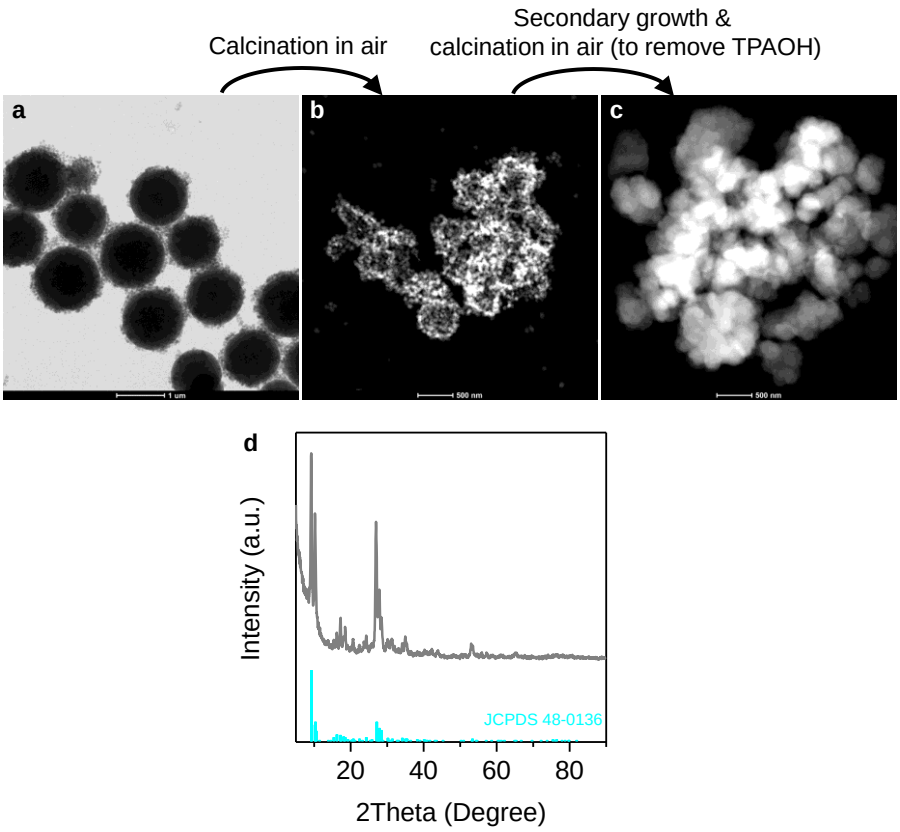

Supplementary Fig. 9: Synthesis of ZSM-5 using CSs and ZSM-5 (feeding Si/Al = 100) nanocrystals and following the same synthetic procedures as for Fe_2O_3@S-1 DSHSs. (a) TEM image of CS@ZSM-5 colloids, (b) STEM-HAADF image of ZSM-5 nanocrystal stacked sphere (obtained by calcination of CS@ZSM-5 colloids in air), (c) STEM-HAADF image and (d) XRD patterns of ZSM-5 (obtained by secondary growth of the ZSM-5 nanocrystal stacked sphere, followed by calcination in air).

Note: This is a control experiment, demonstrating that the transformation from M^{n+}-CSs to hollow MO spheres is vital for forming the final MO@ZEO DSHSs structure. If CSs were used instead of Fe^{3+}-CSs, no hollow Fe_2O_3 spheres were formed to prop up the attached zeolite nanocrystals (plot b). Finally, only solid sphere-like zeolite formed (plot c). The solid sphere-like ZSM-5 (plot c and d) was further used to synthesize hs-Fe_2O_3+H-ZSM-5 and Fe_2O_3/H-ZSM-5 for catalytic syngas conversion.

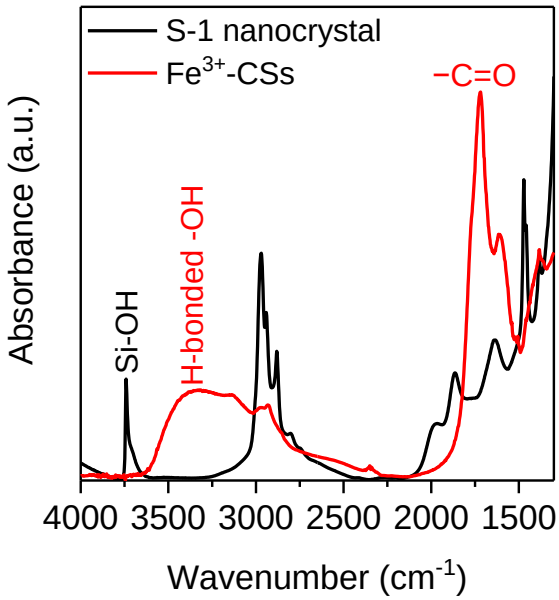

Supplementary Fig. 10: Evidence for the hydrogen bonding between S-1 nanocrystals and Fe^{3+}-CSs. FT-IR spectra of S-1 nanocrystals (with TPAOH) and Fe^{3+}-CSs acquired at 150 °C under vacuum conditions.

Note: The intense and sharp IR band at ~ 3740 cm^{-1}, observed in S-1 nanocrystals, is attributed to free terminal Si–OH groups[3]. As CSs were synthesized by hydrothermal polymerization of sucrose, Fe^{3+}-CSs exhibited a typical hydrogen-bonded O−H stretching mode, characterized by an intense and broad IR band at ~ 3350 cm^{-1}.[4]

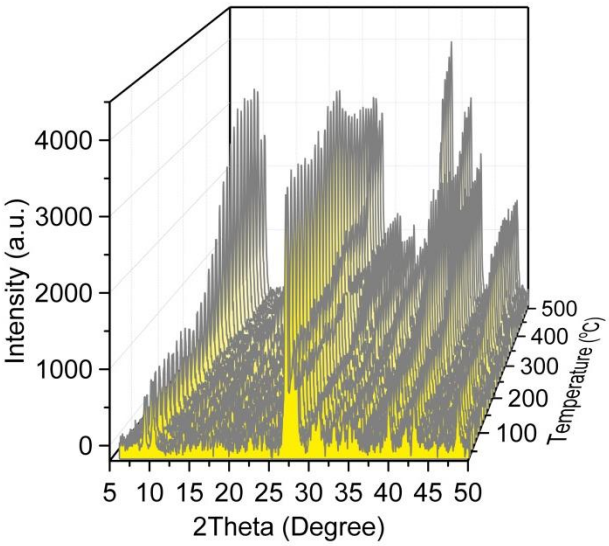

Supplementary Fig. 11: In-situ XRD spectra acquired during calcination of Fe^{3+}-CS@S-1 colloidal particles in O_2/Ar (1/4, v/v) gas flow.

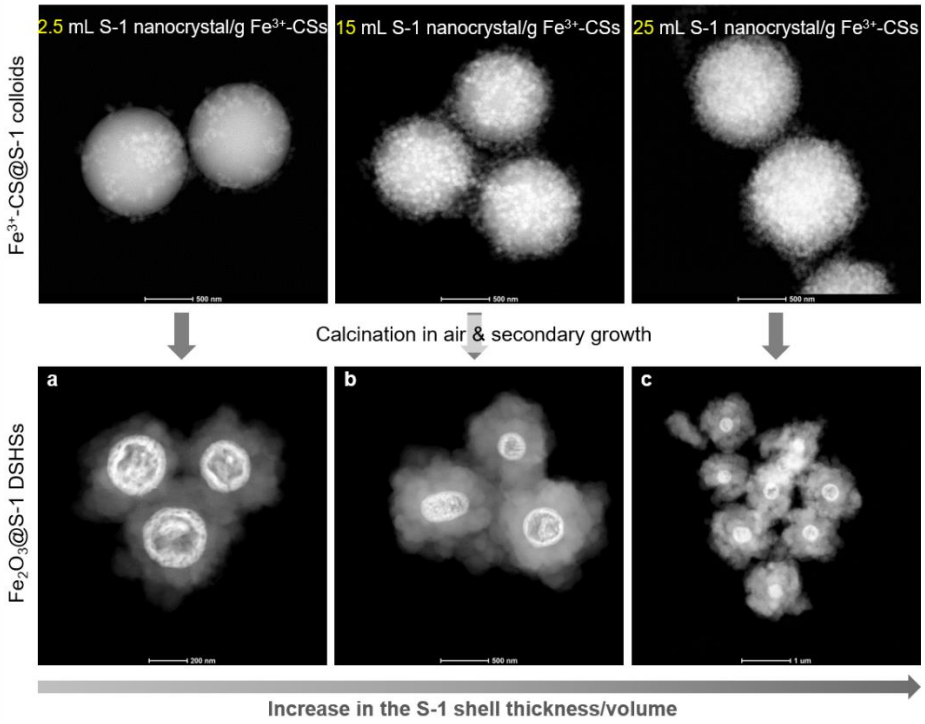

Supplementary Fig. 12: Tuning the S-1 shell thickness/volume by adjusting the quantity ratio of the S-1 nanocrystal to Fe^{3+}-CSs. STEM-HAADF image of the synthesized Fe^{3+}-CS@S-1 colloids and Fe_2O_3@S-1 DSHSs, using (a) 2.5, (b) 15, and (c) 25 mL S-1 nanocrystal suspension (1 wt% in distilled water) for each gram of Fe^{3+}-CSs. Other synthetic conditions: 1.5 M $Fe(NO_3)_3$ for doping 1.2 μm CSs at room temperature; secondary growth of the S-1 shell at 95 °C for 1 day.

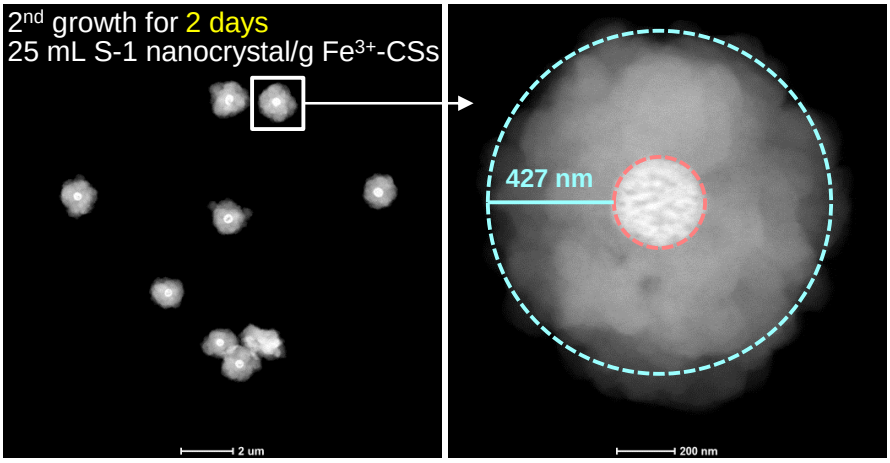

Supplementary Fig. 13: Effect of the secondary growth duration on the S-1 shell thickness. STEM-HAADF image of Fe_2O_3@S-1 DSHSs prepared with two days' secondary growth of the S-1 shell.

Note: The only difference between this sample (2 days' secondary growth of S-1 shell) and the sample (1 day) in Fig. 4a3 lies in the secondary growth duration. Extending the secondary growth time from 1 day to 2 days leads to only a slight increase in the S-1 shell thickness from ca. 400 nm (Fig. 4a3) to ca. 427 nm (Supplementary Fig. 13).

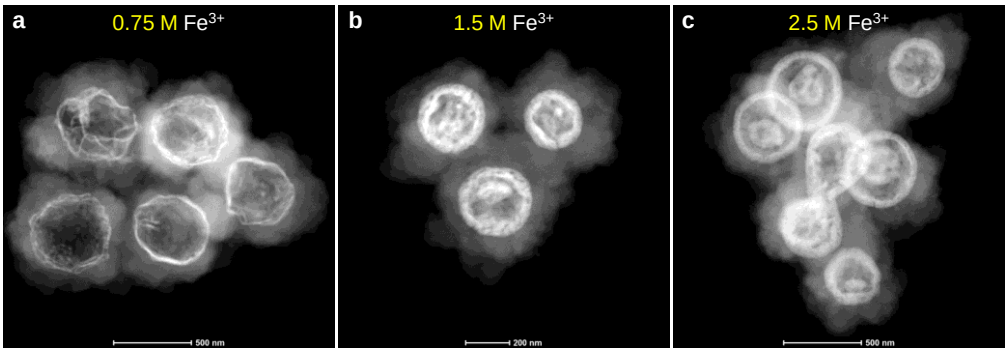

Supplementary Fig. 14: Tuning the Fe_2O_3 shell thickness by adjusting the concentration of the $Fe(NO_3)_3$ doping solution. STEM-HAADF image of Fe_2O_3@S-1 DSHSs synthesized using (a) 0.75, (b) 1.5 and (c) 2.5 M $Fe(NO_3)_3$ as the doping solution. Other synthetic conditions: doping 1.2 µm CSs at room temperature; 2.5 mL S-1 nanocrystal suspension (1 wt% in distilled water) for each gram of Fe^{3+}-CSs; secondary growth of the S-1 shell at 95 °C for 1 day.

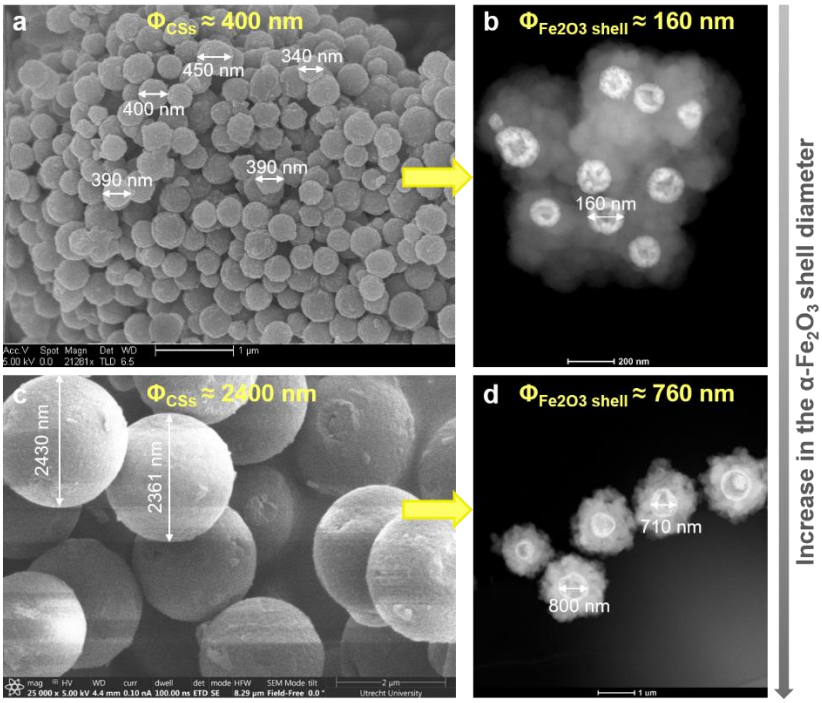

Supplementary Fig. 15: Tuning the Fe_2O_3 shell diameter by using differently sized CSs. SEM images of CSs with diameters of ca. (a) 0.4 μm and (c) 2.4 μm. They were synthesized by hydrothermal polymerization of 60 mL 1.5 M sucrose (aq.) at 190 °C for 90 and 135 min, respectively. (b and d) STEM-HAADF image of Fe_2O_3@S-1 DSHSs synthesized with these two differently sized CSs as the precursor. Other synthetic conditions: 1.5 M $Fe(NO_3)_3$ for doping CSs at room temperature; 15 mL S-1 nanocrystal suspension (1 wt% in distilled water) for each gram of Fe^{3+}-CSs; secondary growth of the S-1 shell at 95 °C for 1 day.

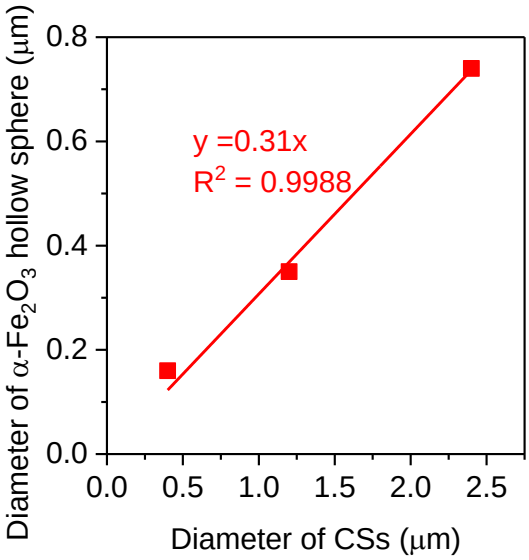

Supplementary Fig. 16: Relation of the mean diameter of the hollow Fe_2O_3 sphere in the resultant Fe_2O_3@S-1 DSHSs to the mean diameter of CSs used.

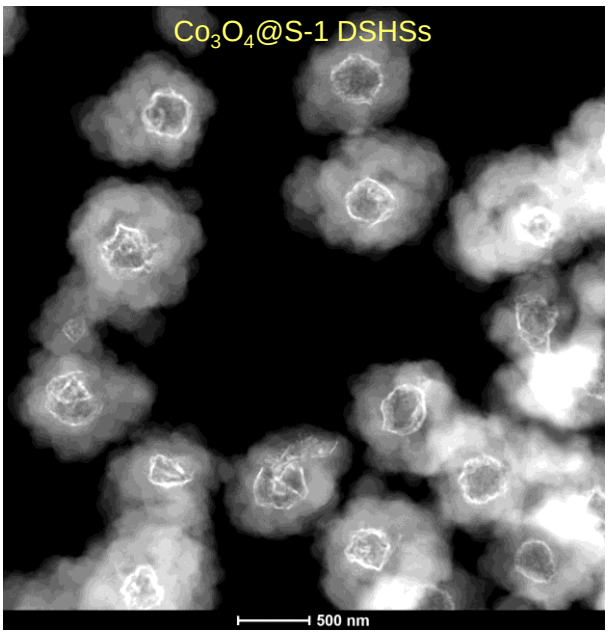

Supplementary Fig. 17: STEM-HAADF image of the synthesized Co_3O_4@S-1 DSHSs. Synthetic conditions: 1.0 M $Co(NO_3)_2$ for doping 1.2 μm CSs at room temperature; 15 mL S-1 nanocrystal suspension (1 wt% in distilled water) for each gram of Co^{2+}-CSs; secondary growth of the S-1 shell at 95 °C for 1 day.

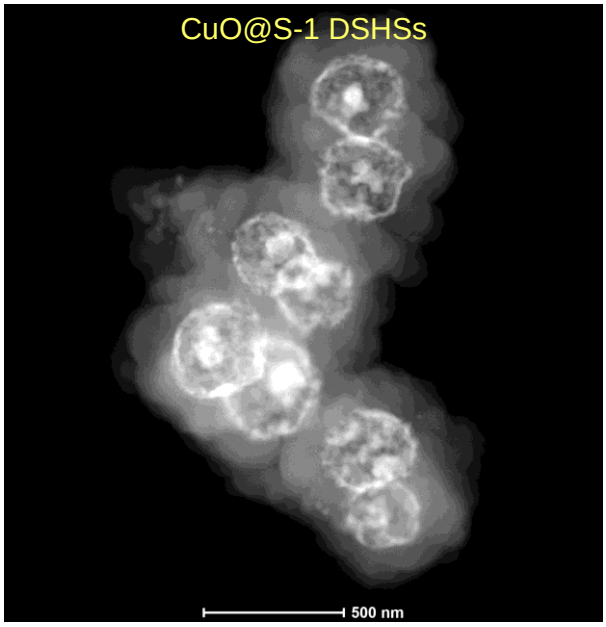

Supplementary Fig. 18: STEM-HAADF image of the synthesized CuO@S-1 DSHSs. Synthetic conditions: 1.5 M $Cu(NO_3)_2$ for doping 1.2 μm CSs at room temperature; 2.5 mL S-1 nanocrystal suspension (1 wt% in distilled water) for each gram of Cu^{2+}-CSs; secondary growth of the S-1 shell at 95 °C for 1 day.

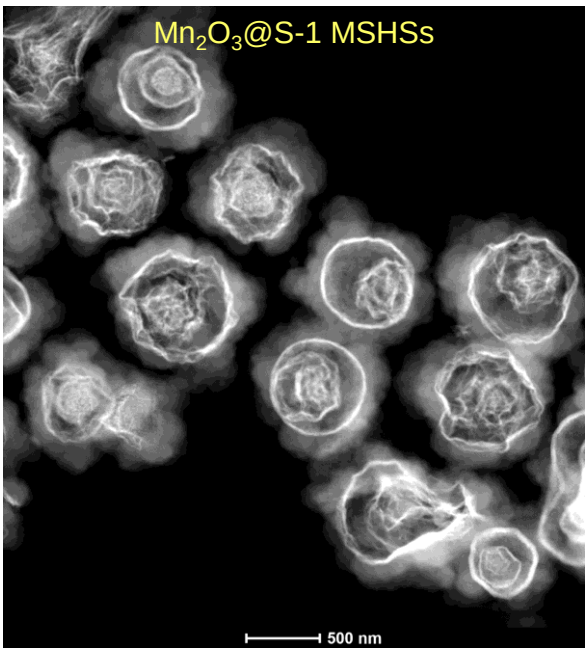

Supplementary Fig. 19: STEM-HAADF image of the synthesized Mn_2O_3@S-1 MSHSs. Synthetic conditions: 0.5 M $Mn(NO_3)_2$ for doping 1.2 μm CSs at 35 °C; 2.5 mL S-1 nanocrystal suspension (1 wt% in distilled water) for each gram of Mn^{2+}-CSs; secondary growth of the S-1 shell at 95 °C for 1 day.

Note: It should be noted that the particular formation of triple-shelled and quadruple-shelled Mn_2O_3 hollow spheres (Fig. 4d3 and Supplementary Fig. 19) is due to the enrichment of Mn species inside Mn^{2+}-CSs, caused by performing the doping process at a higher temperature (35 °C). According to the Arrhenius equation[5], a higher temperature value results in a higher diffusion rate coefficient and, hence, more Mn^{2+} ions can be adsorbed by CSs. This indicates that the number of concentric hollow MO spheres is likely controllable by governing various factors (e.g., metal precursor concentration, doping temperature, doping duration, and solvent property) impacting the adsorption efficiency of metal cations by CSs.

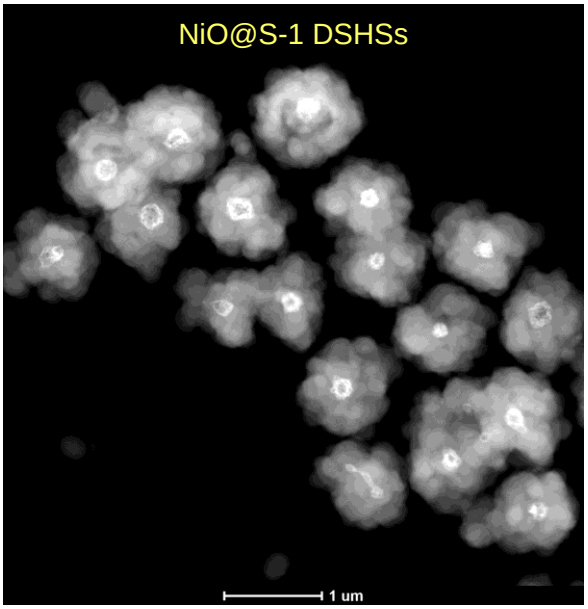

Supplementary Fig. 20: STEM-HAADF image of the synthesized NiO@S-1 DSHSs. Synthetic conditions: 1.0 M $Ni(NO_3)_2$ doping 0.4 μm CSs at room temperature; 25 mL S-1 nanocrystal suspension (1 wt% in distilled water) for each gram of Ni^{2+}-CSs; secondary growth of the S-1 shell at 95 °C for 1 day.

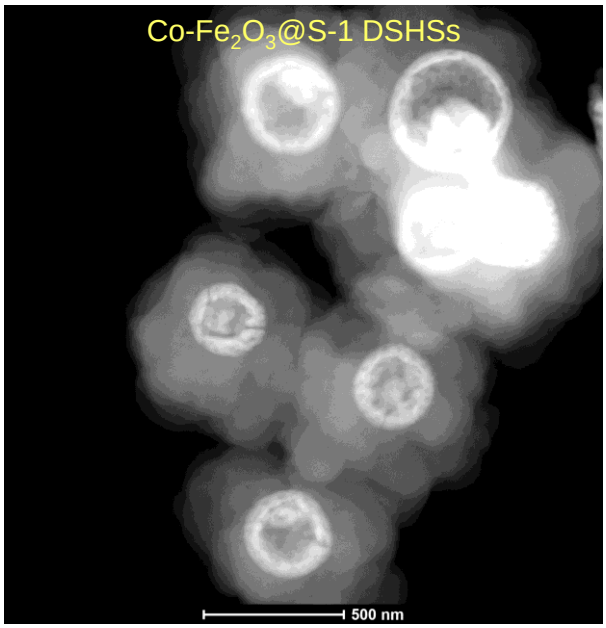

Supplementary Fig. 21: STEM-HAADF image of the synthesized Co-Fe_2O_3@S-1 DSHSs. Synthetic conditions: 1.5 M $Fe(NO_3)_3$ and 1.0 M $Co(NO_3)_2$ for doping 1.2 μm CSs at room temperature; 15 mL S-1 nanocrystal suspension (1 wt% in distilled water) for each gram of Fe^{3+}/Co^{2+}-CSs; secondary growth of the S-1 shell at 95 °C for 1 day.

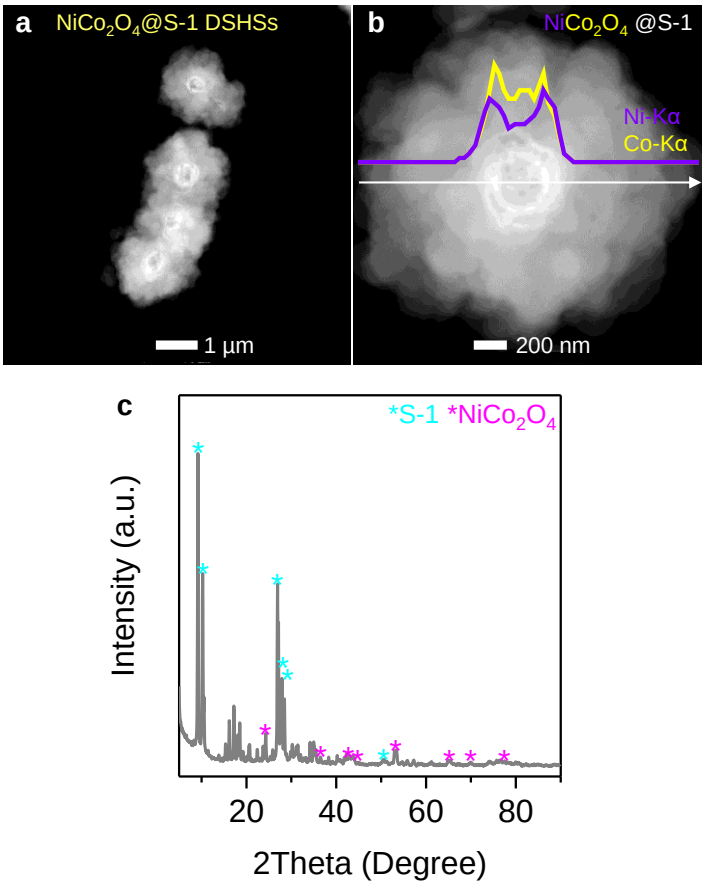

Supplementary Fig. 22: Characterization of the synthesized $NiCo_2O_4$@S-1 DSHSs. (a and b) STEM-HAADF images with EDS line-scan spectra and (c) XRD patterns of the synthesized $NiCo_2O_4$@S-1 DSHSs. Synthetic conditions: 1.0 M $Ni(NO_3)_2$ and 2.0 M $Co(NO_3)_2$ for doping 2.4 μm CSs at room temperature; 25 mL S-1 nanocrystal suspension (1 wt% in distilled water) for each gram of Ni^{2+}/Co^{2+}-CSs; secondary growth of the S-1 shell at 95 °C for 1 day.

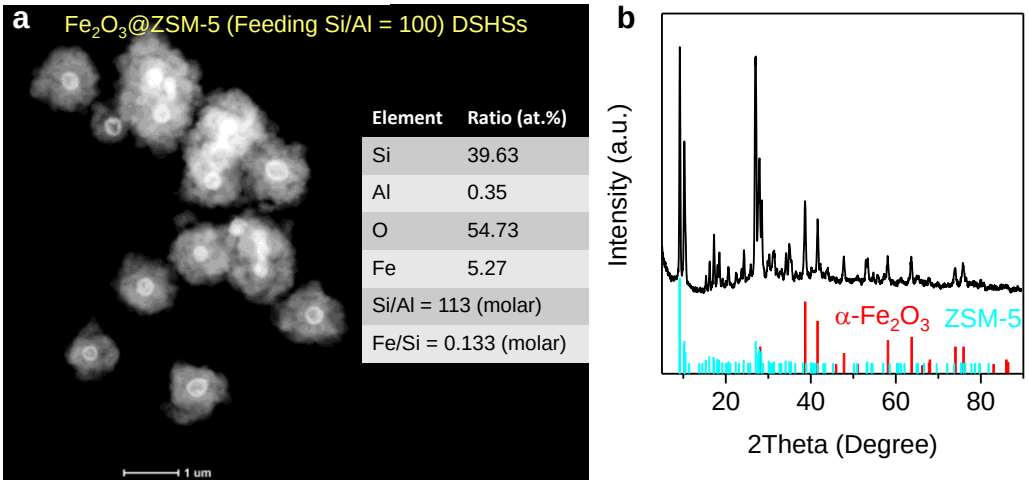

Supplementary Fig. 23: Characterization of the synthesized Fe_2O_3@ZSM-5 (feeding Si/Al = 100) DSHSs. (a) STEM-HAADF image and EDS quantification results; (b) XRD patterns. Synthetic conditions: 1.5 M $Fe(NO_3)_3$ solution for doping 1.2 μm CSs at room temperature; 15 mL ZSM-5 (feeding Si/Al = 100, Supplementary Fig. 24) nanocrystal suspension (1 wt% in distilled water) for each gram of Fe^{3+}-CSs; secondary growth of the ZSM-5 shell at 95 °C for 1 day (the Si/Al ratio of the nutrient sol is 100).

Note: The mass fraction of Fe_2O_3 to ZSM-5 in this material was determined to be 1:9 by the X-ray fluorescence analysis.

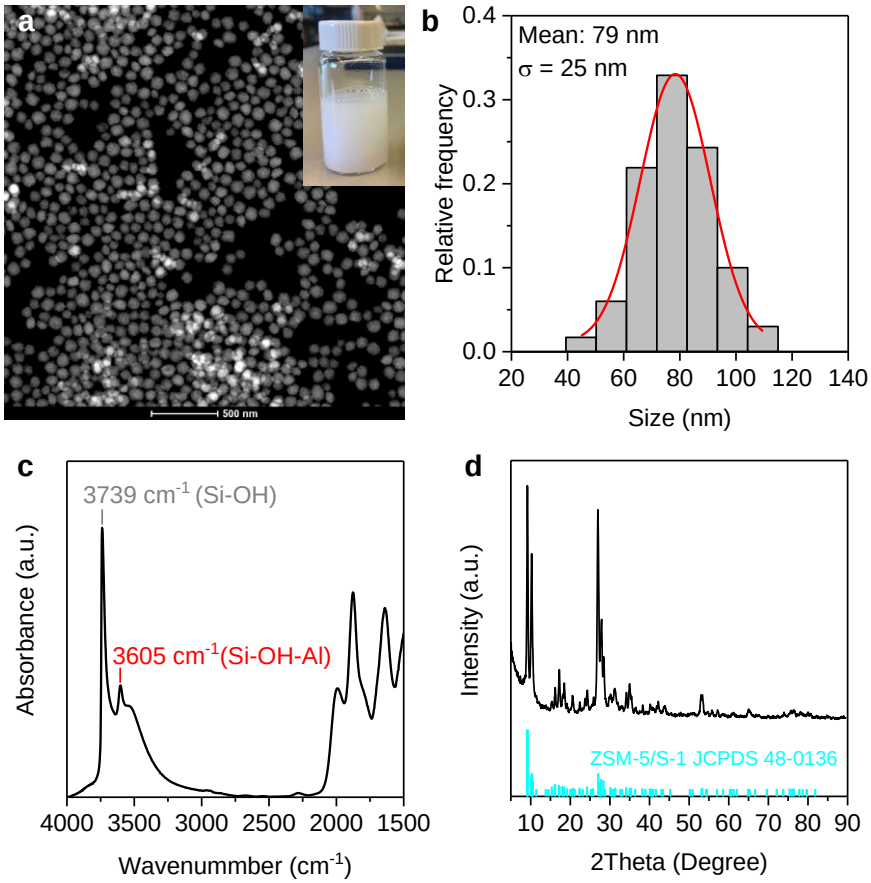

Supplementary Fig. 24: Characterization of ZSM-5 (feeding Si/Al = 100) nanocrystals. (a) STEM-HAADF image and (b) size distribution of the ZSM-5 (feeding Si/Al = 100) nanocrystals. (c) IR spectra (acquired at 150 °C under vacuum conditions) and XRD patterns of the H-ZSM-5 nanocrystals (after removing TPAOH by calcination and conversion into the H-form). The inlet in panel a shows the photograph of 1 wt% ZSM-5 nanocrystal suspension in distilled water.

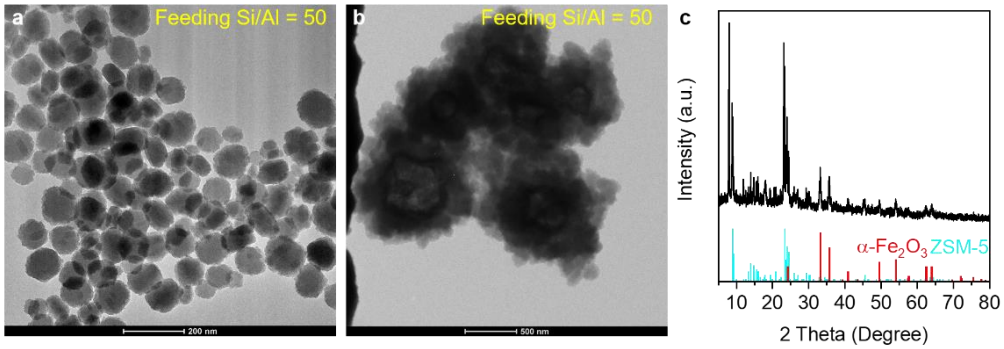

Supplementary Fig. 25. Synthesis of Fe_2O_3@ZSM-5 (Si/Al = ca. 50) DSHSs. TEM images of (a) the prepared ZSM-5 (feeding Si/Al = 50) nanocrystals and (b) Fe_2O_3@ZSM-5 DSHSs (feeding Si/Al = 50). (c) XRD pattern of the latter material. Synthetic conditions: 1.5 M $Fe(NO_3)_3$ solution for doping 1.2 μm CSs at room temperature; 15 mL 1 wt% ZSM-5 (feeding Si/Al = 50) nanocrystal suspension (plot a) for each gram of Fe^{3+}-CSs; secondary growth of the ZSM-5 shell in a nutrient sol (Si/Al = 50) at 95 °C for 1 day.

Note: The actual Si/Al ratio in the prepared Fe_2O_3@ZSM-5 DSHSs was determined to be 57 by the X-ray fluorescence analysis. We note that MO@ZSM-5 DSHSs with a Si/Al ratio of around 25 or lower were not attainable at present, due to the failure in the synthesis of the corresponding zeolite nanocrystals by the present method.

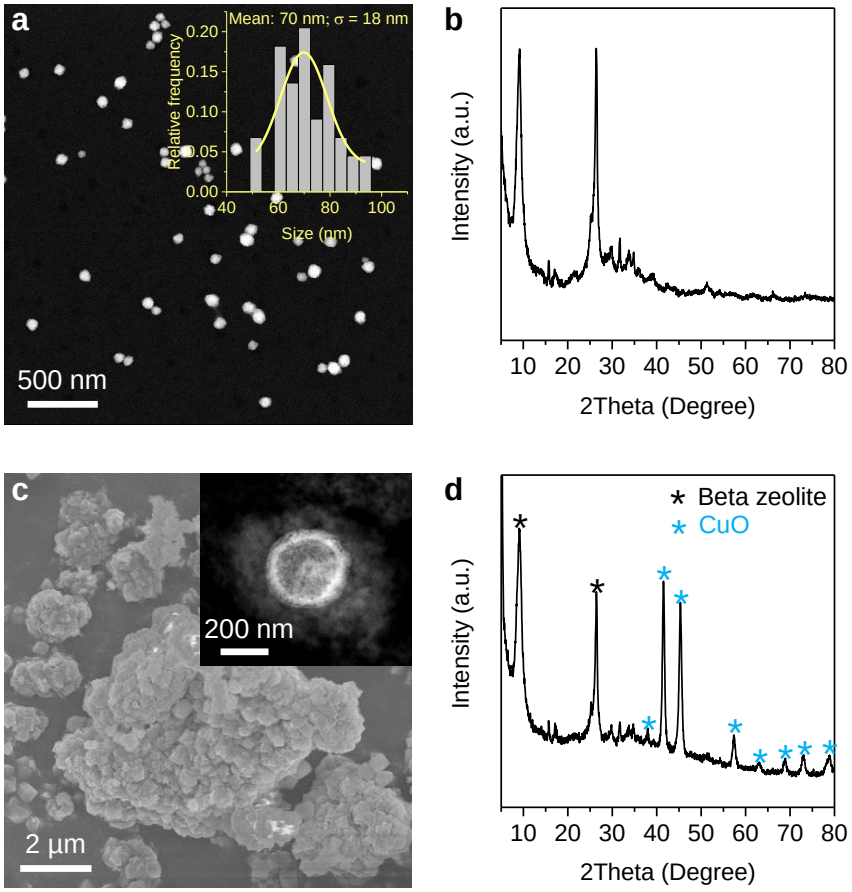

Supplementary Fig. 26: Characterization of the synthesized Si-Beta zeolite nanocrystals and CuO@Beta DSHSs. (a) STEM-HAADF image, size distribution and XRD patterns of the Si-Beta zeolite nanocrystals. (c) SEM and STEM-HAADF image, and (d) XRD patterns of CuO@Si-Beta zeolite DSHSs. Synthetic conditions for CuO@Si-Beta zeolite DSHSs: 2.0 M $Cu(NO_3)_2$ for treating 1.2 µm CSs at room temperature; 15 mL Si-Beta zeolite nanocrystal (panel a and b) suspension (1 wt% in distilled water) for each gram of Cu^{2+}-CSs; secondary growth of the Si-Beta zeolitic shell at 170 °C for 15 h in a rotating Teflon lined stainless steel autoclave.

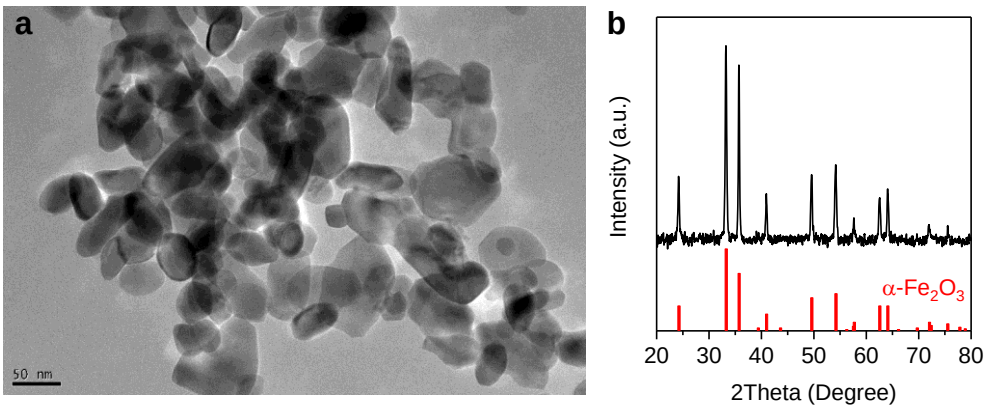

Supplementary Fig. 27: Characterization of bulk Fe_2O_3. (a) TEM image and (b) XRD patterns of bulk Fe_2O_3. All peaks of the XRD patterns are matched with the phase of α-Fe_2O_3 (JCPDS No. 33-0664). Note that the XRD patterns of bulk Fe_2O_3 were acquired with a Cu Kα radiation source (λ = 1.54056Å), while the XRD patterns of most other samples were acquired with a Co Kα irradiation source (λ = 1.789 Å).

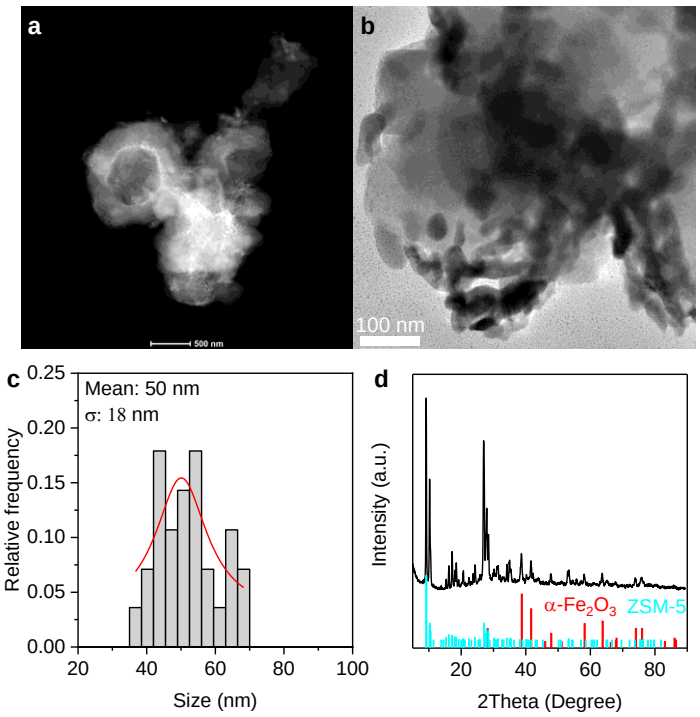

Supplementary Fig. 28: Characterization of Fe_2O_3/ZSM-5 prepared by a typical impregnation method. (a) STEM-HAADF image and (b) TEM image of Fe_2O_3/ZSM-5. (c) Size distribution of Fe_2O_3 in Fe_2O_3/ZSM-5. (d) XRD pattern of Fe_2O_3/ZSM-5.

Note: The mass fraction of Fe_2O_3 to ZSM-5 in this material was determined to be 1:9 by the X-ray fluorescence analysis.

Supplementary Table 2. Catalytic performances of iron catalysts and bifunctional catalysts in syngas conversion.

Catalyst	X_{CO} (%)	S_{CO2} (%)	Hydrocarbon selectivity (%)					C_{5-11} faction (%)		
			CH_4	$C_{2-4}^{=}$	C_{2-4}^{0}	C_{5-11}	C_{12+}	*aro.*	*iso.*	*n.*
b-Fe_2O_3	8.0	16.0	20.0	28.1	18.8	33.1	0.0	0	12.1	87.9
hs-Fe_2O_3	49.0	27.0	12.3	28.8	19.5	38.4	1.0	0	10.5	89.5
Fe_2O_3@S-1 DSHSs	62.3	24.3	16.8	25.5	21.0	36.7	0.0	0	16.3	81.7
hs-Fe_2O_3+H-ZSM-5	50.3	24.2	18.9	12.8	24.0	44.2	0.0	42.1	41.0	17.0
Fe_2O_3/H-ZSM-5	57.0	24.0	15.0	16.0	14.0	55.0	0.0	23.5	51.3	25.2
Fe_2O_3@H-ZSM-5 DSHSs	79.0	25.6	5.7	15.9	14.1	64.0	0.3	34.7	51.3	14.0

Reaction conditions: W_{cat} = 0.03 (for catalysts without acid sites) or 0.3 g (for bifunctional catalysts), H_2/CO = 2/1, F_{syngas} = 30 mL min^{-1}, T = 300 °C, P = 3 MPa, Time on stream = 15 h. C_{2-4}^{0}, $C_{2-4}^{=}$, C_{5-11} and C_{12+} denote C_2−C_4 paraffins, C_2−C_4 olefins, C_5−C_{11} hydrocarbons and products with carbon numbers greater than or equal to 12, respectively. *Aro.*, *iso.* and *n.* denote aromatics, *iso*-alkanes/*iso*-alkenes and *n*-alkanes/*n*-alkenes in C_{5-11} range hydrocarbons.

Note: It should be mentioned that the H-ZSM-5 component in hs-Fe_2O_3+H-ZSM-5 and Fe_2O_3/H-ZSM-5 were made using CSs as the template and following the same synthetic procedures as for Fe_2O_3@H-ZSM-5 DSHSs (Supplementary Figs. 9c and d). This is to ensure the same properties of H-ZSM-5 (Si/Al = ca. 100) in hs-Fe_2O_3+H-ZSM-5, Fe_2O_3/H-ZSM-5 and Fe_2O_3@H-ZSM-5 DSHSs, allowing for a fair comparison between them. Also, the Fe_2O_3/H-ZSM-5 mass proportion of hs-Fe_2O_3+H-ZSM-5 and Fe_2O_3/H-ZSM-5 was tailored to be the same as that of Fe_2O_3@H-ZSM-5 DSHSs (1:9), according to the X-ray fluorescence analysis.

Supplementary Table 3. S_{BET} values of the catalysts.

Sample	S_{BET} (m^2/g)
b-Fe_2O_3	18.1
hs-Fe_2O_3	61.2
Fe_2O_3@S-1 DSHSs	342.9
hs-Fe_2O_3+H-ZSM-5	300.2
Fe_2O_3/H-ZSM-5	278.8
Fe_2O_3@H-ZSM-5 DSHSs	311.5

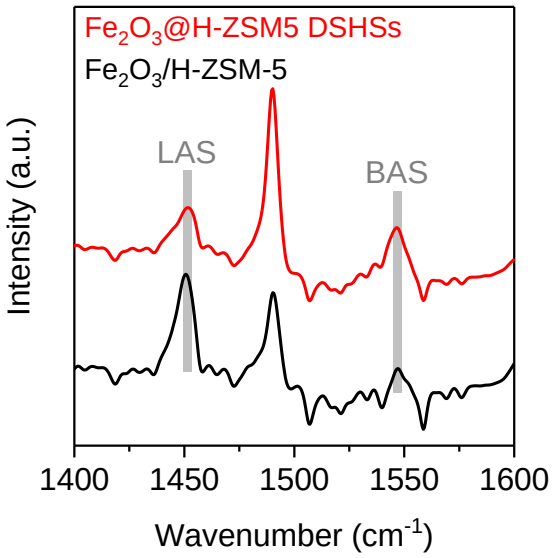

Supplementary Fig. 29: Comparison of the acid properties between Fe_2O_3@H-ZSM-5 DSHSs and Fe_2O_3/H-ZSM-5. Pyridine adsorbed IR spectra of Fe_2O_3@H-ZSM-5 DSHSs and Fe_2O_3/H-ZSM-5. The characteristic peaks of adsorbed pyridine on Brønsted acid sites (BAS) and Lewis acid sites (LAS) appear at 1545 cm^{-1} and 1450 cm^{-1}, respectively.

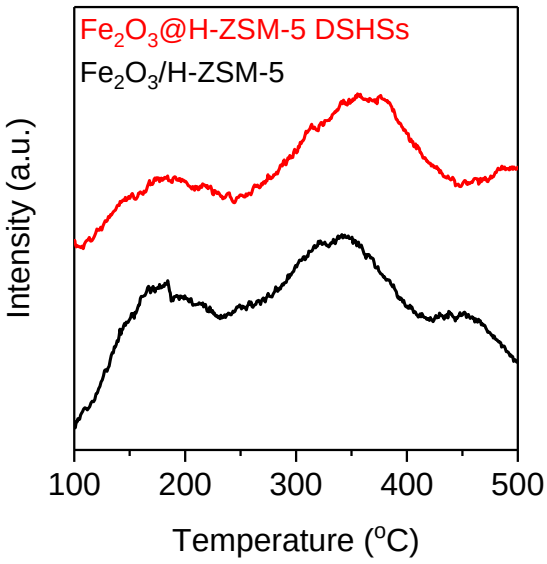

Supplementary Fig. 30: NH_3-TPD profiles of Fe_2O_3@H-ZSM-5 DSHSs and Fe_2O_3/H-ZSM-5.

Supplementary Table 4. Effect of the H-ZSM-5 shell thickness on the catalytic performance of Fe_2O_3@H-ZSM-5 DHSHs in syngas conversion.

H-ZSM-5 thickness	$m_{Fe2O3}/m_{H\text{-}ZSM\text{-}5}$[a]	X_{CO} (%)	S_{CO2} (%)	Hydrocarbon selectivity (%)				
				CH_4	$C_{2-4}^{=}$	C_{2-4}^{0}	C_{5-11}	C_{12+}
ca.100 nm (Supplementary Fig. 31a)[b]	1:3	74.1	29.9	13.0	35.6	13.0	38.4	0
ca. 290 nm (Supplementary Fig. 31b)[b]	1:9	79.0	25.6	5.7	15.9	14.1	64.0	0.3
ca.480 nm (Supplementary Fig. 31c)[b]	1:20	65.6	28.4	22.9	12.3	29.4	35.4	0

[a]Determined by the X-ray fluorescence analysis.

[b]The Fe_2O_3 shell thickness was fixed at ca. 50 nm.

Reaction conditions: W_{cat} = 0.3 g, H_2/CO = 2/1, F_{syngas} = 30 mL min^{-1}, T = 300 °C, P = 3 MPa, Time on stream = 15 h. C_{2-4}^{0}, $C_{2-4}^{=}$, C_{5-11} and C_{12+} denote C_2−C_4 paraffins, C_2−C_4 olefins, C_5−C_{11} hydrocarbons and products with carbon numbers greater than or equal to 12, respectively.

Note: The Fe_2O_3/H-ZSM-5 proportion in Fe_2O_3@H-ZSM-5 DHSHs is controllable by tuning the thickness of one layer (e.g., HZSM-5) while fixing the thickness of the other layer (e.g., Fe_2O_3). Upon a constant Fe_2O_3 layer thickness of approximately 50 nm, adjustment of the quantity ratio of H-ZSM-5 nanocrystal to Fe^{3+}-CSs during the synthesis increased the H-ZSM-5 shell thickness from approximately 100 to 290 and to 480 nm (Supplementary Fig. 31), resulting in the decrease of the mass ratio of Fe_2O_3 to H-ZSM-5 from 1:3 to 1:9 and to 1:20 (Supplementary Table 4). The proportion of Fe_2O_3 to H-ZSM-5 significantly impacted the performance of Fe_2O_3@H-ZSM-5 DHSHs (Supplementary Table 4 and Fig. 32). All the three catalysts exhibited high CO conversions (> 65%). Fe_2O_3@H-ZSM-5 DHSHs with a $m_{Fe2O3}/m_{H\text{-}ZSM\text{-}5}$ ratio of 1:9 exhibited the optimal performance in gasoline production. When the H-ZSM-5 shell thickness decreased to ca. 100 nm, the C_2–C_4 olefins selectivity increased notably, as a result of insufficient acid sites to catalyze the oligomerization reaction. Too thick a H-ZSM-5 shell (ca. 480 nm) was found to result in high selectivities of methane and C_2–C_4 alkanes, which is most likely due to the mass transfer limitation. The optimal Fe_2O_3/H-ZSM-5 mass ratio (1:9) was close to other reported results[6,7].

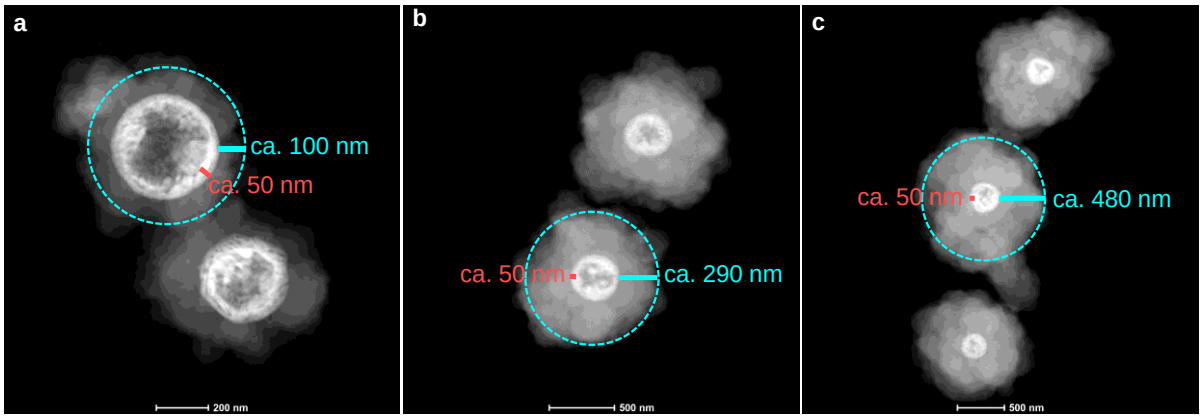

Supplementary Fig. 31. Control of the Fe_2O_3/H-ZSM-5 proportion in Fe_2O_3@H-ZSM-5 DHSHs by tuning the HZSM-5 shell thickness while fixing the thickness of the Fe_2O_3 layer. STEM images of the prepared Fe_2O_3@H-ZSM-5 DHSHs with a ca. 50-nm thick Fe_2O_3 layer and an approximately (a) 100, (b) 290 and (c) 480 nm thick H-ZSM-5 shell. The concentration of the $Fe(NO_3)_3$ doping solution was fixed at 1.5 M, while 2.5 mL, 15 mL and 30 mL H-ZSM-5 nanocrystal suspension (1 wt% in distilled water) were used in a, b and c, respectively, for each gram of Fe^{3+}-CSs.

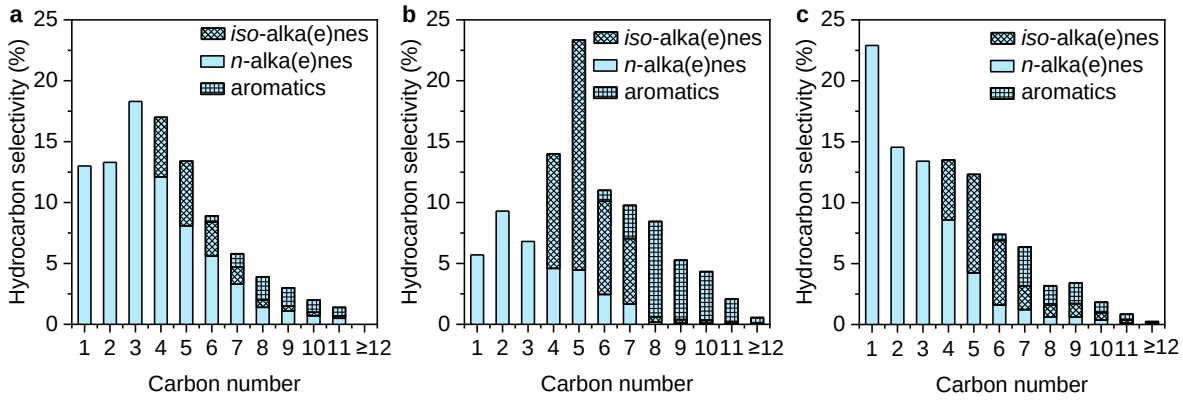

Supplementary Fig. 32. Distribution of the hydrocarbon products over Fe_2O_3@H-ZSM-5 DHSHs with different H-ZSM-5 shell thicknesses. (a) ca. 100 nm (Supplementary Fig. 31a); (b) ca. 290 nm (Supplementary Fig. 31b); and (c) ca. 480 nm (Supplementary Fig. 31c).

Supplementary Table 5. Comparison between the performances of the state-of-the-art Fe-zeolite-based bifunctional catalysts in gasoline production via FTS.

Catalyst	T (°C)	X_{CO} (%)	S_{CO2} (%)	Hydrocarbon selectivity (%)				Ref.
				CH_4	C_{2-4}	C_{5-11}	*aro.*	
Fe-Pd/H-ZSM-5	310	75.7	21.4	22.1	28.4	49.5	15.8	[6]
FeMn@H-ZSM-5	320	51.9	36.6	15.0	22.9	62.1	47.1	[8]
FeZnNa/H-ZSM-5	340	88.8	27.5	9.6	26.6	63.8	50.6	[9]
Fe_3O_4@MnO_2+HOL-HZSM-5	320	90.3	45.0	5.0	25.0	70.0	56.6	[10]
Fe_3O_4@MnO_2+HOL-HZSM-5	320	69.3	47.6	4.0	15.6	80.4	55.2	[11]
Fe_2O_3@H-ZSM-5 DSHSs	300	79.0	25.6	5.7	30.0	64.0	22.2	This work

Note: For the C_5–C_{11} range hydrocarbons, the best bifunctional iron-zeolite catalysts (Fe_3O_4@MnO_2+hollow HZSM-5) could offer a high selectivity of around 70–80%[10,11]. However, around 69–81% of the C_5–C_{11} products were mixed aromatics. This does not meet the environmental requirement for high-quality gasoline that the aromatics content should be restricted to lower than 35%[12,13]. The formation of aromatics is thermodynamically favorable under harsh reaction conditions, which is one major reason that most bifunctional catalysts with high selectivity of C_5–C_{11} hydrocarbons often produce aromatics rather than *iso*-alkanes. The aromatics fraction in C_5–C_{11} hydrocarbons produced by our Fe_2O_3@H-ZSM-5 DSHSs catalyst was 34.7%, and the fraction of *iso*-alkanes and *iso*-alkenes was as high as 51.3% (Supplementary Table 2). Although the C_5–C_{11} selectivity of Fe_2O_3@H-ZSM-5 DSHSs is slightly lower than that of the best bifunctional catalysts reported in the literature, the composition of liquid hydrocarbons was much closer to the requirement of practical gasoline. This is the ascendancy of our catalyst over the state-of-the-art Fe-zeolite-based bifunctional catalysts in the aspect of gasoline production performance via FTS. Note that the performance of Fe_2O_3@H-ZSM-5 DSHSs is expected to be further enhanced by the diameter refinement and/or proper doping of promoters (e.g., Mn, Na or K) into the Fe_2O_3 layer in the future.

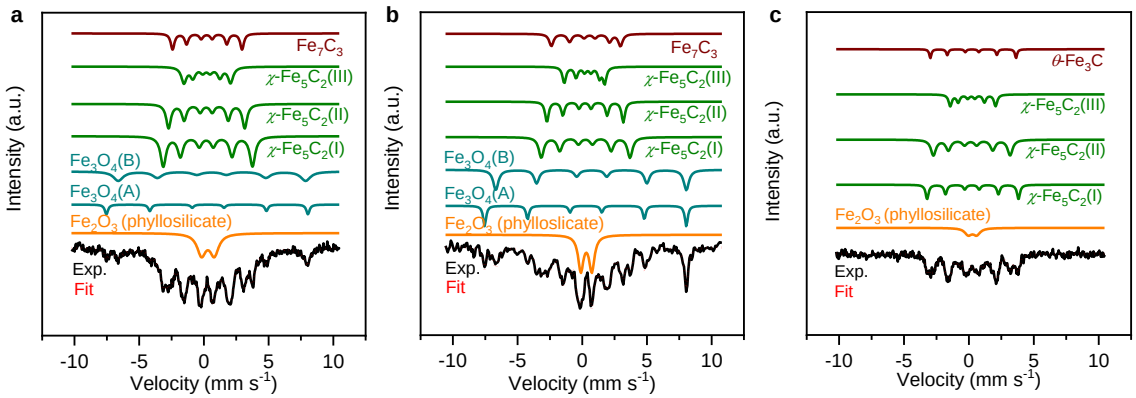

Supplementary Fig. 33. Detection of the formed iron carbides (FeC_x) in the bifunctional catalysts. Mössbauer spectra of (a) Fe_2O_3@H-ZSM-5 DSHSs, (b) Fe_2O_3/H-ZSM-5 and (c) hs-Fe_2O_3+H-ZSM-5 following FTS for 45 h.

Supplementary Table 6. Phase quantification of iron species in reacted Fe_2O_3@H-ZSM-5 DSHSs, Fe_2O_3/H-ZSM-5 and hs-Fe_2O_3+H-ZSM-5 for 45 h on stream.

Reacted catalysts	Iron species	Ratio (%)	Ratio (%)
Fe_2O_3@H-ZSM-5 DHSHs	Fe_2O_3	14.8±2.6	Carbides: 65.9 Oxides: 34.1
	Fe_3O_4(I)	5.0±1.8	
	Fe_3O_4(II)	14.3±4.2	
	χ-Fe_5C_2(I)	25.7±4.0	
	χ-Fe_5C_2(II)	12.9±2.7	
	χ-Fe_5C_2(III)	18.0±8.6	
	Fe_7C_3	9.2±6.4	
Fe_2O_3/H-ZSM-5	Fe_2O_3	17.4±2.5	Carbides: 52.4 Oxides: 47.6
	Fe_3O_4(I)	11.0±3.2	
	Fe_3O_4(II)	19.2±4.7	
	χ-Fe_5C_2(I)	19.0±6.7	
	χ-Fe_5C_2(II)	13.0±8.7	
	χ-Fe_5C_2(III)	10.6±3.4	
	Fe_7C_3	9.8±7.5	
hs-Fe_2O_3+H-ZSM-5	Fe_2O_3	11.5±3.8	Carbides: 88.5 Oxides: 11.5
	χ-Fe_5C_2(I)	21.3±8.9	
	χ-Fe_5C_2(II)	38.8±8.1	
	χ-Fe_5C_2(III)	19.1±4.5	
	Θ-Fe_3C	9.3±9.1	

Note: hs-Fe_2O_3+H-ZSM-5 was ahead of others in terms of the FeC_x content because of an excellent iron dispersion and segregation of iron and H-ZSM-5. Fe_2O_3@H-ZSM-5 DSHSs exhibited a lower FeC_x content than hs-Fe_2O_3+H-ZSM-5 due likely to the Fe_2O_3@H-ZSM-5 core-shell structure. The formation of FeC_x were the least in the case of Fe_2O_3/H-ZSM-5 likely due to the strong Fe-HZSM-5 chemical interactions that may cause the formation of iron silicates or aluminates at high temperatures that are hard to be reduced or carbonized[14,15].

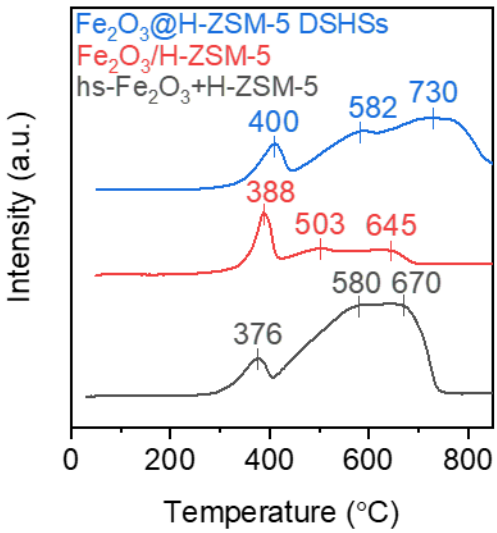

Supplementary Fig. 34. H_2 temperature-programmed reduction (H_2-TPR) profiles of the prepared bifunctional catalysts.

Note: The H_2-TPR profiles exhibit several hydrogen consumption peaks, attributing to the reduction of different iron species. The low-temperature peaks at 380–400 °C were attributed to the reduction of hematite (Fe_2O_3) to magnetite (Fe_3O_4), while the high-temperature peaks corresponded to the transformation process of Fe_3O_4 → FeO → Fe. The reducibility of iron species in the bifunctional catalysts followed the order of hs-Fe_2O_3+H-ZSM-5 > Fe_2O_3@H-ZSM-5 DSHSs > Fe_2O_3/H-ZSM-5, in line with the carbonization result (Supplementary Table 6).

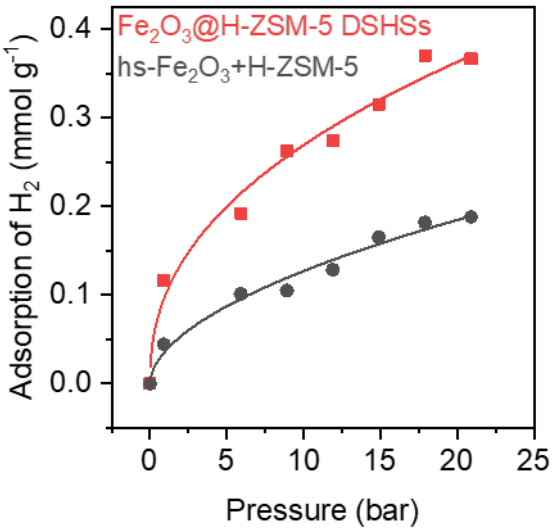

Supplementary Fig. 35. H_2 adsorption isotherm of Fe_2O_3@H-ZSM-5 DSHSs and hs-Fe_2O_3+H-ZSM-5.

Note: The surface areas of Fe_2O_3@H-ZSM-5 DSHSs and hs-Fe_2O_3+H-ZSM-5 were almost the same (Supplementary Table 2), and these two materials included the same hollow-sphere Fe_2O_3. The only difference lay in that the H-ZSM-5 in Fe_2O_3@H-ZSM-5 DSHSs and hs-Fe_2O_3+H-ZSM-5 were hollow-sphere and solid-sphere, respectively. Thus, the significantly higher H_2 adsorption capacity in the case of Fe_2O_3@H-ZSM-5 DSHSs was most likely due to the “cage” effect of the hollow H-ZSM-5 sphere. The enrichment effect of a hollow chamber was also reported by Ma *et. al*[16], which increased the local concentration of H_2 around the active sites, resulting in an accelerated reaction rate and an improved catalytic performance.

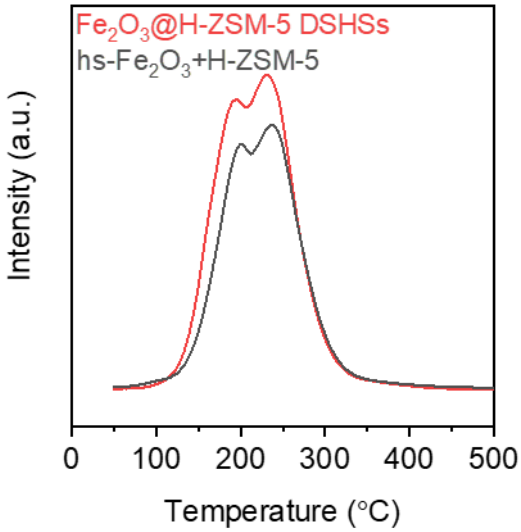

Supplementary Fig. 36. C_3H_6-TPD profiles of Fe_2O_3@H-ZSM-5 DSHSs and hs-Fe_2O_3+H-ZSM-5. The C_3H_6-TPD intensity was normalized to the same acid density (obtained from NH_3-TPD).

Note: Fe_2O_3@H-ZSM-5 DSHSs exhibited a larger uptake of C_3H_6 (a possible reaction intermediate in gasoline production via FTS) than hs-Fe_2O_3+H-ZSM-5, in keeping with the H_2 adsorption isotherms (Supplementary Fig. 34). This indicates again that the hollow-sphere H-ZSM-5 as the outer shell in Fe_2O_3@H-ZSM-5 DSHSs could enrich the reactants and reaction intermediates.

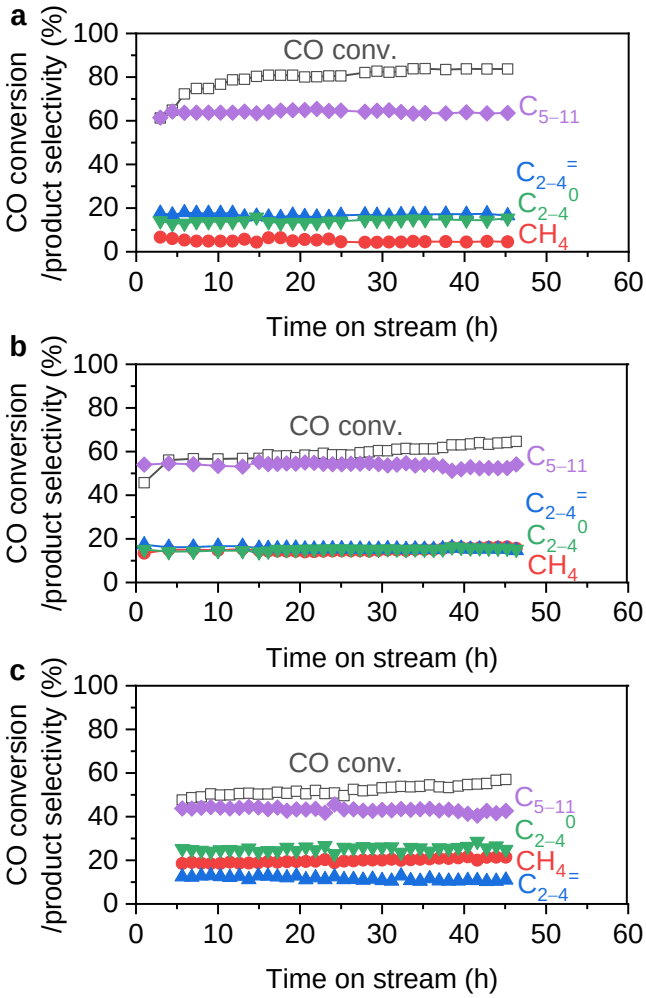

Supplementary Fig. 37. Catalytic stabilities of (a) Fe_2O_3@H-ZSM-5 DSHSs, (b) Fe_2O_3/H-ZSM-5 and (c) hs-Fe_2O_3+H-ZSM-5.

Note: It was found that after a short induction time of 10 h, the performance of Fe_2O_3@H-ZSM-5 DHSHs became stable and no catalyst deactivation was observed during 45 h on steam (plot a). An induction period was required possibly because of the core-shell architecture that slightly decelerated the carburization of the inner Fe_2O_3 layer into active carbide phases. The CO conversion and C_5–C_{11} selectivity maintained at about 80% and 64%, respectively. The hs-Fe_2O_3+H-ZSM-5 and Fe_2O_3/H-ZSM-5 catalysts also exhibited stable performances in syngas conversion (plot c; Supplementary Table 7).

Supplementary Table 7. Catalytic performance over the bifunctional catalysts of different times on stream.

Catalyst	*Time on stream (h)*	X_{CO} (%)	S_{CO2} (%)	Hydrocarbon selectivity (%)					$C_{5\text{-}11}$ faction (%)		
				CH_4	$C_{2-4}^{=}$	C_{2-4}^{0}	C_{5-11}	C_{12+}	*aro.*	*iso.*	*n.*
hs-Fe_2O_3+H-ZSM-5	15	50.3	24.2	18.9	12.8	24.0	44.2	0.0	42.1	41.0	17.0
hs-Fe_2O_3+H-ZSM-5	45	57.1	26.0	21.4	11.0	25.0	42.6	0.0	40.0	42.0	18.0
Fe_2O_3/H-ZSM-5	15	57.0	24.0	15.0	16.0	14.0	55.0	0.0	23.5	51.2	25.3
Fe_2O_3/H-ZSM-5	45	64.1	26.1	16.3	15.3	15.7	52.4	0.4	23.0	51.6	25.4
Fe_2O_3@H-ZSM-5 DSHSs	15	79.0	25.6	5.7	15.9	14.1	64.0	0.3	34.7	51.3	14.0
Fe_2O_3@H-ZSM-5 DSHSs	45	83.6	26.0	5.0	16.0	15.4	63.5	0.2	34.0	51.0	14.9

Reaction conditions: W_{cat} = 0.3 g, H_2/CO = 2/1, F_{syngas} = 30 mL min^{-1}, T = 300 °C, P = 3 MPa. C_{2-4}^{0}, $C_{2-4}^{=}$, C_{5-11} and C_{12+} denote C_2−C_4 paraffins, C_2−C_4 olefins, C_5−C_{11} hydrocarbons and products with carbon numbers greater than or equal to 12, respectively. *Aro.*, *iso.* and *n.* denote aromatics, *iso*-hydrocarbons and *n*-hydrocarbons in C_{5-11} range hydrocarbons.

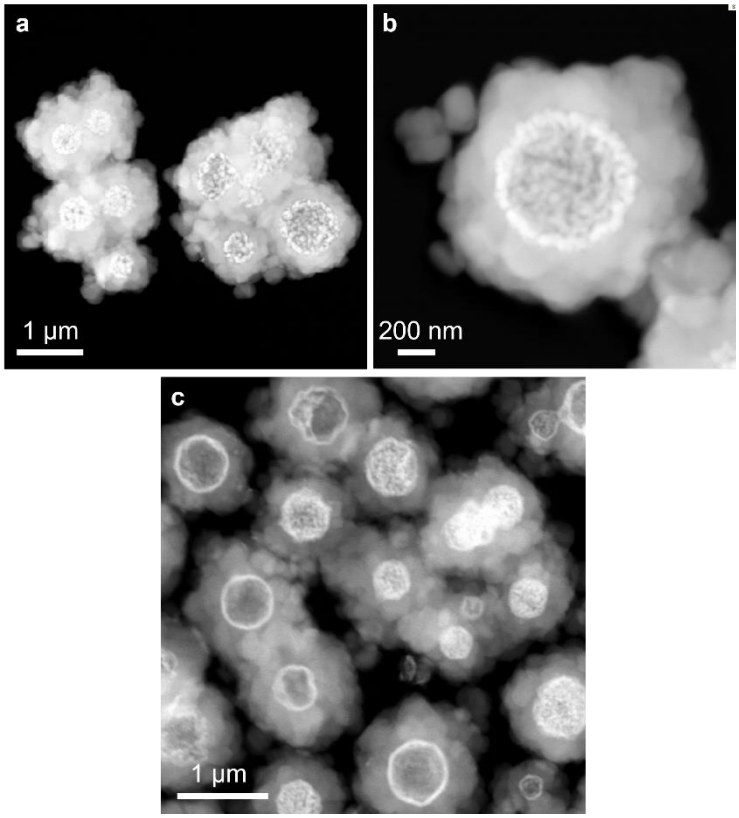

Supplementary Fig. 38. Structural stability of Fe_2O_3@H-ZSM-5 DSHSs after FTS reaction and regeneration. STEM images of Fe_2O_3@H-ZSM-5 DSHSs (a and b) after FTS for 45 h and (c) further regeneration by annealing at 500 °C in air for 2 h.

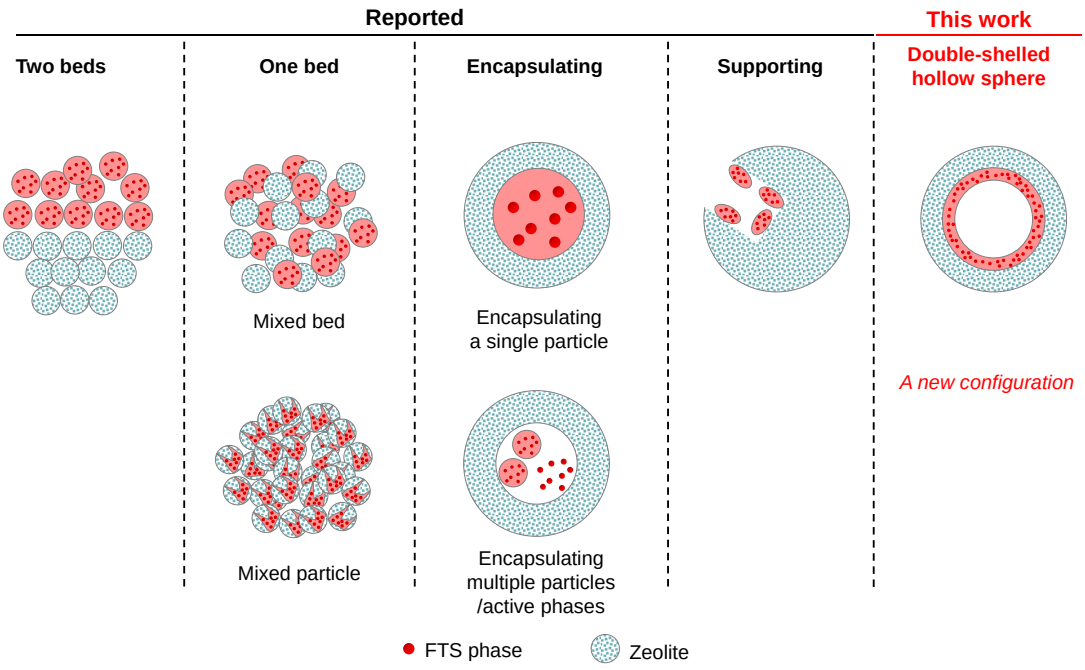

Supplementary Fig. 39. Schematic representation of different configurations that FTS phases and the zeolite may have with respect to on another in bifunctional systems.

Note: Our work provides a brand-new configuration between FTS phases and the zeolite compared with the existing ones[17], in bifunctional systems.

Supplementary references

1. Wang, J. Y. *et al.* Multi-shelled metal oxides prepared via an anion-adsorption mechanism for lithium-ion batteries. *Nat. Energy* **1**, 16050 (2016).

2. Wang, Q., Li, H., Chen, L. & Huang, X. Monodispersed hard carbon spherules with uniform nanopores. *Carbon* **39**, 2211–2214 (2001).

3. Góra-Marek, K., Derewiński, M., Sarv, P. & Datka, J. IR and NMR studies of mesoporous alumina and related aluminosilicates. *Catal. Today* **101**, 131–138 (2005).

4. Auer, B., Kumar, R., Schmidt, J. & Skinner, J. Hydrogen bonding and Raman, IR, and 2D-IR spectroscopy of dilute HOD in liquid D_2O. *P. Natl. Acad.Sci.* **104**, 14215–14220 (2007).

5. Laidler, K. J. The development of the Arrhenius equation. *J. Chem. Ed.* **61**, 494 (1984).

6. Yan, Q. *et al.* Synthesis of Aromatic-Rich Gasoline-Range Hydrocarbons from Biomass-Derived Syngas over a Pd-Promoted Fe/HZSM-5 Catalyst. *Energy Fuels* **28**, 2027–2034 (2014).

7. Weber, J. L., Dugulan, I., de Jongh, P. E. & de Jong, K. P. Bifunctional Catalysis for the Conversion of Synthesis Gas to Olefins and Aromatics. *ChemCatChem* **10**, 1107–1112 (2018).

8. Xu, Y. *et al.* Yolk@Shell FeMn@Hollow HZSM-5 Nanoreactor for Directly Converting Syngas to Aromatics. *ACS Catal.* **11**, 4476–4485 (2021).

9. Zhao, B. *et al.* Direct Transformation of Syngas to Aromatics over Na-Zn-Fe_5C_2 and Hierarchical HZSM-5 Tandem Catalysts. *Chem* **3**, 323–333 (2017).

10. Xu, Y. *et al.* Selective Conversion of Syngas to Aromatics over Fe_3O_4@MnO_2 and Hollow HZSM-5 Bifunctional Catalysts. *ACS Catal.* **9**, 5147–5156 (2019).

11. Xu, Y., Wang, J., Ma, G., Lin, J. & Ding, M. Designing of Hollow ZSM-5 with Controlled Mesopore Sizes To Boost Gasoline Production from Syngas. *ACS Sustain. Chem. Eng.* **7**, 18125–18132 (2019).

12. Li, N. *et al.* High-Quality Gasoline Directly from Syngas by Dual Metal Oxide–Zeolite (OX-ZEO) Catalysis. *Angew. Chem. Int. Ed.* **58**, 7400–7404 (2019).

13. Ramirez, A., Sarathy, S. M. & Gascon, J. CO_2 Derived E-Fuels: Research Trends, Misconceptions, and Future Directions. *Trends Chem.* **2**, 785–795 (2020).

14. Latham, K., Round, C. I. & Williams, C. D. Synthesis, further characterisation and catalytic activity of iron-substituted zeolite LTL, prepared using tetrahedral oxo-anion species. *Microporous Mesoporous Mater* **38**, 333–344 (2000).
15. Torres Galvis, H. M. *et al.* Iron Particle Size Effects for Direct Production of Lower Olefins from Synthesis Gas. *J. Am. Chem. Soc.* **134**, 16207–16215 (2012).
16. Yao, D. *et al.* A high-performance nanoreactor for carbon-oxygen bond hydrogenation reactions achieved by the morphology of nanotube-assembled hollow spheres. *ACS Catal.* **8**, 1218–1226 (2018).
17. Sartipi, S., Makkee, M., Kapteijn, F. & Gascon, J. Catalysis engineering of bifunctional solids for the one-step synthesis of liquid fuels from syngas: a review. *Catal. Sci. Technol.* **4**, 893–907 (2014).